A Computational Methodology for Simulating the Pervasive Failure of Structures Under Extreme Loading Conditions[1]

SAND2007-5288C

Joseph Bishop
Solid Mechanics / Structural Dynamics Sciences Department
Sandia National Laboratories[2]
Albuquerque, NM 87185-0372
jebisho@sandia.gov

ABSTRACT

Dynamic material fracture and overall structural failure is a highly nonlinear process involving complex material constitutive behavior, material softening, localization, surface generation, and ubiquitous contact. In weapons effects analysis most often the extent of failure is pervasive in the sense that a multitude of cracks are nucleating, propagating in arbitrary directions, coalescing, and branching. A pure Lagrangian computational methodology has been developed to simulate the pervasive failure of materials and structures. A key aspect of this methodology is that fracture surfaces are allowed to nucleate only at the inter-cell boundaries of a randomly seeded Voronoi tessellation of the domain. Each Voronoi cell is formulated as a finite element, and the Voronoi tessellation becomes the finite-element mesh. The randomly seeded Voronoi tessellation provides an unbiased computational basis for representing fracture surfaces. In an attempt to properly handle material softening and localization, cohesive tractions are dynamically inserted at the new surfaces. Solution behavior with mesh refinement is studied for the example of a concrete structure striking a rigid wall.

1 INTRODUCTION

Possible structural responses from a weapon assault can range from intact vibrational response to complete fragmentation with secondary impacts. The structure transitions from a continuum to a discontinuum through crack propagation. The extent of fracturing is typically pervasive in the sense that a multitude of cracks are nucleating, propagating in arbitrary directions, coalescing, and branching. Currently, there is a very limited set of computational tools available that can attempt to simulate the pervasive failure of structures. Common and often unsatisfactory industrial techniques include 'element death' in Lagrangian finite-element codes and 'void insertion' in hydrocodes. The enriched finite-element methods (generalized finite-element method and extended finite-element method) have had success in modeling fracture problems in which the crack topology does not change significantly and loading regimes in which linear elastic fracture mechanics is applicable [1,2]. Once crack-branching and crack coalescence phenomena appear, the prospect of modeling a multitude of arbitrary three-dimensional intersecting cracks becomes untenable. A variety of meshless or particle methods have been developed in the past fifteen years with the goal of modeling extreme deformation including pervasive failure [3]. Examples include spherical-particle hydrodynamics [4], element-free Galerkin [5], reproducing kernel method [6], cracked-particles [7], peridynamics [8], particle in element [9], and element to particle conversion [10]. Each of these methods has had varying degrees of success in modeling dynamic crack propagation and even pervasive failure. However, many of these methods are plagued by a number of issues including computational cost and integration with existing finite-element technology. Ortiz and coworkers [11-16] have pursued the concept of using traditional finite element methods but only allowing fracture surfaces to nucleate and propagate along the inter-element faces of tetrahedra. At the inception of material softening and localization, the mesh connectivity is modified to reflect the new surface and a cohesive traction with a softening behavior is dynamically inserted. The use of a tetrahedral mesh, albeit unstructured, is potentially biased with respect to edge and face orientation which could lead to nonobjective numerical predictions. Ideally, the face structure would be completely random to remove any bias. Herein, the approach of Ortiz is adopted but instead of using tetrahedral elements, the finite elements are derived from the cells of a randomly seeded Voronoi tessellation of the domain. The randomly seeded Voronoi tessellation provides an unbiased computational basis for representing fracture surfaces. Also, the resulting polyhedral cells have a number of desirable properties including convexity and relatively large included angles. The latter property is expected to result in increased robustness in large deformation analyses. The use of randomly seeded Voronoi tessellations has been used extensively by Bolander and coworkers in their development of lattice models [17-20].

The intersection of general surfaces can result in arbitrarily small subdomains whose surface topology is inappropriate for further computation. The restriction of only allowing new surfaces to form at interelement faces provides a necessary regularization of the resulting domain and surface topologies. For example, variational methods for solving the governing equations of motion, e.g. the finite-element method, require that the domain have a Lipschitz continuous boundary. Thus, as the original domain fractures and disassociates into

---

[1] Presented at the International Symposium on Interaction of the Effects of Munitions with Structures 12.1 (hosted by DTRA), September 17-21, 2007, Orlando, FL.

[2] Sandia is a multi-program laboratory operated by Sandia Corporation, a Lockheed Martin Company, for the United States Department of Energy's National Nuclear Security Administration under Contract DE-AC04-94AL85000.

subdomains, each subdomain needs to have a Lipschitz continuous boundary as well. Also, the restriction of only allowing new surfaces to form at interelement faces provides *a priori* the constraint on minimum edge size and subsequent critical-time step necessary in an explicit-dynamic numerical solution. It remains to be shown that this finite basis set for representing fracture surfaces is large enough to enable predictive simulations of pervasive failure problems. Note that the use of this methodology for modeling dynamic crack propagation results in a time varying domain whose measure or volume is continuous in time. This is not the case in a number of particle methods whose continuum representation evolves into a collection of spheres. (Recall that the theoretical maximum packing for equi-sized sphere is only 74%.) This continuity of volume in time is very important in confined fragmentation problems (e.g. rock blasting, wrapped concrete columns under seismic or blast loading). Note that the smallest fragment of the proposed method is the individual element itself, not a node or particle. Thus, each element or fragment is fully deformable and capable of consistently representing a continuum, even under reconsolidation. Also, the smallest fragment can carry angular momentum in addition to linear momentum. Again, this is not the case with most particle methods.

Any computational methodology that strives to model pervasive failure must not only include the ability to numerically represent the progression of a body from a continuum description to a discontinuum description but also regularize the governing equations so that the onset of material softening and its progression to a new crack surface results in finite and nonzero energy dissipation. This latter condition derives from the requirement that the computational methodology be objective such that the simulation results do not depend on subjective properties of the model such as mesh design. A necessary condition for objectivity is that the numerical approximation converges with refinement. Without convergence to the necessary 'engineering accuracy', numerical results and predictions are non-objective and thus suspect, rendering validation, uncertainty quantification efforts, and general use in engineering design suspect as well. It is well known that the failure to regularize the governing equations can result in pathological 'mesh dependence' and non-objective results [21,40]. Two common methods for regularizing the governing equations are the dynamic insertion of cohesive tractions at the *inception* of material softening [11-16], and the use of integral-form nonlocal material models [24-27,40,44] with the insertion of new crack surfaces only upon the *completion* of material softening and thus final localization of damage. As a first step only the dynamic insertion of cohesive tractions is used herein. The use of an integral-form nonlocal model is under study.

Quasi-brittle materials such as concrete, geomaterials, and toughened ceramics, are characterized by large fracture process zones relative to the structure size with a majority of the fracture process zone undergoing softening due to microcracking, void formation, interface debonding, and frictional slipping [21]. The cohesive model of the crack mouth provides a good description of this behavior. Thus, the familiar K field used in fracture mechanics does not apply at moderate structure sizes, and no field enrichment or calculation of stress intensity factors is necessary. For this reason only quasi-brittle material behavior is studied for this initial phase of the research.

This paper is organized as follows. Section 2 gives an overview of the computational methodology and its five key components. Section 3 presents a two dimensional example with a discussion on convergence for engineering quantities-of-interest. Section 4 discusses a number of possible 'next steps' and challenges.

2 COMPUTATIONAL METHODOLOGY

The proposed computational methodology for simulating pervasive failure may be described as a Lagrangian explicit-dynamic displacement-based finite-element method with dynamic connectivity. The methodology consists of the following components: (1) randomly seeded Voronoi tessellation (mesh) of the domain, (2) each Voronoi cell formulated as a finite element using the Reproducing Kernel Method (RKM), (3) fracture allowed only at element faces (edges) and subsequent dynamic change in mesh connectivity, (4) use of either a nonlocal material model (integral form) or the dynamic insertion of cohesive tractions to regularize the governing equations, and (5) robust and efficient contact algorithm. Each component will be described in the following sections.

2.1 Random Voronoi Tessellation

Bolander and coworkers [17-20] have used random Voronoi tessellations in spring-lattice models to simulate quasistatic crack growth in quasibrittle materials and structures. Their methodology for randomizing and regularizing the Voronoi tessellation is adopted here. Voronoi tessellations have a rich history in mathematics and science and have a number of advantageous properties [28]. Given a finite set of points $\{\mathbf{X}_i\}$ or nuclei, the Voronoi diagram is defined as the collection of regions or cells V_i where

$$V_i = \bigcap_{i \neq j} \left\{ \mathbf{X} \mid d(\mathbf{X}_i, \mathbf{X}) < d(\mathbf{X}_j, \mathbf{X}) \right\} \tag{1}$$

Each point belonging to the Voronoi cell i is closer to nucleus i than all other nuclei. Note that each Voronoi cell is defined as the intersection of half-spaces and is thus convex. An example of a Voronoi cell is shown in Figure 1c. To generate a random Voronoi tessellation with some control on the regularity of the resulting cells (e.g. aspect ratios near one), the approach of Bolander [17] is followed. For a given characteristic length h, the nuclei are randomly and sequentially placed in the domain with a constraint on minimum distance between nuclei until the maximum packing threshold is reached. The constraint on minimum distance between particles is enforced by merely discarding those nuclei that violate the constraint. An example nuclei distribution is shown in Figure 1a. The cell nuclei are used to triangulate the domain using the Bowyer-Watson insertion algorithm resulting in a Delaunay triangulation (Figure 1b) [29,30]. The Voronoi diagram is simply the dual of the Delaunay (Figure 1c) so that the Voronoi cell nuclei are the vertices of the Delaunay triangulation, and the vertices of the Voronoi cells are the circumcenters of the Delaunay triangles. Note that most junctions are triples and the interior angles are approximately 120°, whereas the dual Delaunay triangulation typically has relatively small interior angles. Thus, it is expected that the Voronoi elements will be more robust in large deformation applications. Also, each junction is randomly orientated and thus unbiased. The generation of the Voronoi diagram is straight forward in unbounded domains but is nontrivial near geometrically 'complex' boundaries due to the need for intersection operations.

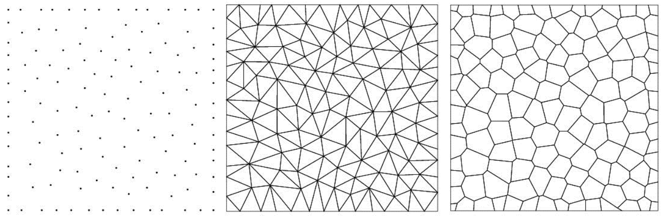

(a) (b) (c)

Figure 1. Methodology used to create the Vornoi tessellation of a domain: (a) random seeding until the theoretical maximum packing is approached with a constraint on minimum seed distance, (b) Delaunay triangulation, and (c) dual Voronoi tessellation.

The Voronoi tessellations typically contain a number of relatively small edges and faces. To regularize the Voronoi tessellation for use in explicit dynamics these small features are simply deleted and the node pairs equivalenced. Figure 2 shows the effect of this mesh regularization step. Histogram plots are also given showing the number of elements with a given number of edges both before and after the deletion of small edges. A majority of elements are hexagons and all elements have four or more edges.

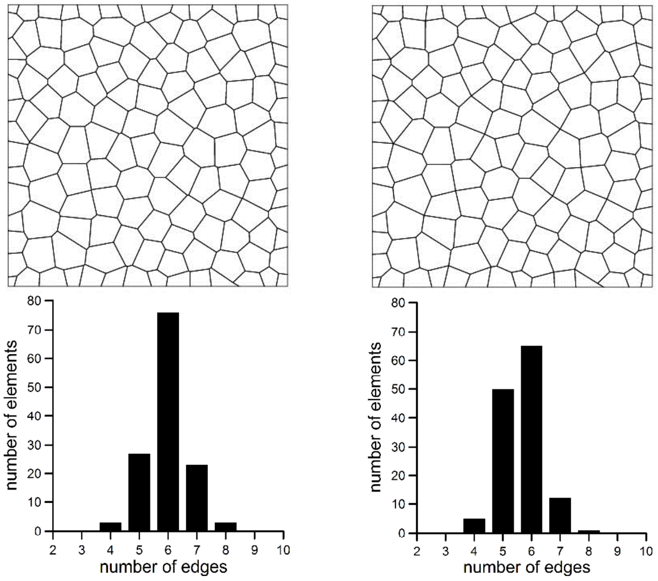

(a) (b)

Figure 2. Regularization of the Voronoi tessellation by removing 'small' edges and equivalencing nodes: (a) raw Voronoi tessellation and (b) Voronoi mesh with constraint on minimum edge size. The histogram of the number of elements with a given number of edges is also given.

2.2 Polyhedral Element Formulation

A general displacement based finite-element formulation for plane faceted polyhedra applicable to large deformations has been achieved by Rashid and coworkers [31]. Their approach consists of developing incompatible polynomial based shape functions that satisfy the minimum properties for convergence. These elements satisfy the Kronecker delta property and are compatible with existing FEA. Idelsohn, *et al* [32] used natural neighbor co-ordinates of a Delaunay tessellation of points to develop a 'meshless' finite element method. Wachspress [33] has used algebraic geometry concepts to develop shape functions on polyhedra. Ghosh and coworkers [46-48] have extensively developed two-dimensional polyhedral elements based on the assumed-stress hybrid finite-element method for modeling composite materials. An alternative formulation is introduced here that uses the reproducing kernel method (RKM) [6] to generate the shape functions. A functional comparison between these various approaches is currently being investigated.

In the reproducing kernel method the nodal *shape* functions $\psi_I(\mathbf{x})$ are generated by first defining a nodal *weight* function $w_I(\mathbf{x})$ that has compact support, has a maximum value at the node, and is smoothly and monotonically decreasing away from the node. In typical applications the nodal weight functions are given circular supports in two dimensions and spherical supports in three dimensions. A number of examples are given in Belytschko, et al [3]. The nodal shape function is then defined as a spatial modulation of the nodal weight function,

$$\psi_I(\mathbf{x}) = C_I(\mathbf{x}) w_I(\mathbf{x}) \tag{2}$$

where the nodal modulation function $C_I(\mathbf{x})$ is chosen so that $\psi_I(\mathbf{x})$ satisfies the desired reproducing and consistency requirements [3]. Let $\mathbf{g}^{\mathrm{T}}(\mathbf{x}) = \{g_1(\mathbf{x}) \quad g_2(\mathbf{x}) \quad g_3(\mathbf{x}) \quad \cdots\}$ be the vector of desired basis functions $g_i(\mathbf{x})$. For linear consistency $\mathbf{g}(\mathbf{x})$ is taken to be $\mathbf{g}^{\mathrm{T}}(\mathbf{x}) = \{1 \quad x \quad y \quad z\}$. Let N be the set of all nodes whose weight function support contains the location $\mathbf{x}$. The shape function reproducing property takes the form

$$\sum_{I \in N} \psi_I(\mathbf{x}) \mathbf{g}(\mathbf{x} - \mathbf{x}_I) = \mathbf{g}(\mathbf{x}) \tag{3}$$

In order to satisfy Eq. (3) $C_I(\mathbf{x})$ is taken to be of the form

$$C_I(\mathbf{x}) = \boldsymbol{a}^{\mathrm{T}}(\mathbf{x})\, \mathbf{g}(\mathbf{x} - \mathbf{x}_I) \tag{4}$$

where $\boldsymbol{a}^{\mathrm{T}}(\mathbf{x}) = \{a_1(\mathbf{x}) \quad a_2(\mathbf{x}) \quad a_3(\mathbf{x}) \quad \cdots\}$ is a vector of unknown scalar valued functions $a_i(\mathbf{x})$. For linear consistency, substituting Eqs. (2) and (4) into Eq. (3) yields

$$\mathbf{A}(\mathbf{x})\, \boldsymbol{a}^{\mathrm{T}}(\mathbf{x}) = \{1 \quad 0 \quad 0 \quad 0\}^{\mathrm{T}} \tag{5}$$

where $\mathbf{A}(\mathbf{x})$ is given by

$$\mathbf{A}(\mathbf{x}) = \sum_{J \in N} w_J(\mathbf{x}-\mathbf{x}_J) \bullet \begin{bmatrix} 1 & x-x_J & y-y_J & z-z_J \\ & (x-x_J)^2 & (x-x_J)(y-y_J) & (x-x_J)(z-z_J) \\ & & (y-y_J)^2 & (y-y_J)(z-z_J) \\ sym & & & (z-z_J)^2 \end{bmatrix} \tag{6}$$

Calculating the inverse of $\mathbf{A}(\mathbf{x})$ allows for the solution of the $a_i(\mathbf{x})$ in Eq. (5) and $C_I(\mathbf{x})$ in Eq. (4). The spatial derivatives of the shape functions can be calculated by direct differentiation of Eqs. (4), (5), and (6) [5].

Now consider the application of this general shape function construction to a Voronoi mesh. First, the nodal weight function is defined as follows. The compact support of node I is chosen to be the union of element domains attached to node I. This support is identical to that used in the standard finite element method. Let this domain be denoted by Ω_I with boundary Γ_I. To define the nodal weight function we solve the following auxiliary problem,

$$\begin{aligned} \nabla^2 w + 1 = 0 \quad & in \quad \Omega_I \\ w = 0 \quad & on \quad \Gamma_I \cap \Gamma = \varnothing \\ \nabla w = 0 \quad & on \quad \Gamma_I \cap \Gamma \neq \varnothing \end{aligned} \tag{7}$$

This auxiliary problem may be efficiently solved using standard boundary element techniques to obtain both w_j and it's derivatives at the integration points, $\mathbf{x}_j$, $j = 1, \ldots, M$. Eqs. (2) through (6) can then be used to calculate the shape function $\psi_I(\mathbf{x})$. By construction, $\psi_I(\mathbf{x}_J) = \delta_{IJ}$, and thus $\psi_I(\mathbf{x})$ satisfies the Kronecker delta property. This result is particularly advantageous and results in a large improvement in computational efficiency and implementation complexity compared to a purely meshless implementation. Also note that along any edge in two dimensions there are only two supporting nodes. Therefore, any shape function varies linearly along an edge. Thus, these polyhedral finite-elements are compatible with the standard first-order isoparametric finite elements. As an example, the weight function and resulting shape function corresponding to an interior node of a regular hexagonal mesh is shown in Figure 3.

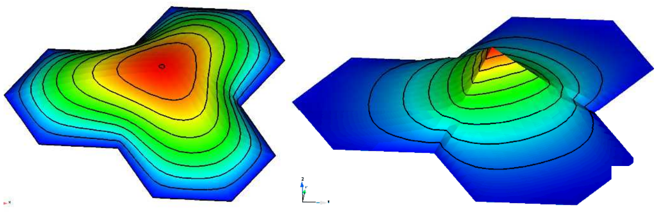

(a) (b)

Figure 3. (a) Nodal weight function for an interior node of a regular hexagonal mesh. The weight functions is obtained by solving the local boundary value problem described by Eq. 7. (b) The shape function resulting from the application of the RKM methodology.

It is important to note that the presented element formulation is not isoparametric, and therefore there is no mapping to a parent element. The shape functions are defined on the reference configuration. Thus, a total Lagrangian formulation of the governing equations is appropriate [34]. The conservation of linear momentum takes the form [5]

$$\mathrm{DIV}\,\mathbf{P} + \rho_o \boldsymbol{f} = \rho_o \ddot{\mathbf{u}} \tag{8}$$

where $\boldsymbol{f}$ is the body force vector per unit mass, $\mathbf{u}$ is the displacement vector, ρ_o is the reference density, $\mathrm{DIV}\,\mathbf{P} \equiv \nabla_o \mathbf{P} : \mathbf{I} = (\partial \mathbf{P} / \partial \mathbf{X}) : \mathbf{I}$, $\mathbf{P}$ is the first Piola-Kirchhoff stress tensor, $\mathbf{I}$ is the identity tensor, and $\mathbf{X}$ represents the position vector in the reference configuration. The weak form of Eq. (8) is

$$\int_{\Omega_o} \rho_o \ddot{\mathbf{u}} \bullet \delta\mathbf{u}\, dV = \int_{\Omega_o} \rho_o \boldsymbol{f} \bullet \delta\mathbf{u}\, dV - \int_{\Omega_o} \mathbf{P} : (\nabla_o \otimes \delta\mathbf{u})\, dV + \int_{\Gamma_o} \mathbf{t}_o \bullet \delta\mathbf{u}\, dA \tag{9}$$

where $\mathbf{t}_o$ is the traction vector per unit initial area, and the displacement vector $\mathbf{u}$ and the virtual displacement vector $\delta\mathbf{u}$ are members of the usual function spaces.

Rashid [31] has proposed a general methodology for developing Gauss points and their weights for integrating the weak form of the equilibrium equation. For the two-dimensional applications presented here, a simple approach is adopted since all of the element domains are star shaped and can be triangulated by connecting the element nodes to the element centroid. Standard Gauss rules for triangles can then be applied. Chen [35] has noted that the use of non-isoparametric element formulations can result in a violation of the discrete form of Gauss's theorem (resulting from Gauss integration) with a subsequent reduction in accuracy and convergence rate. For a given shape function ψ the continuous version of Gauss's theorem over an element subdomain Ω_e with boundary Γ_e and outward unit normal n_i is given by

$$\int_{\Omega_e} \psi_{,i} = \int_{\Gamma_e} \psi\, n_i \tag{10}$$

The discrete form is given by

$$\sum_j \omega_j \psi^j{}_{,i} = \sum_j \omega_j^\Gamma \psi^j n_i \tag{11}$$

where $\psi^j \equiv \psi(\mathbf{x}_j)$, $\mathbf{x}_j$ are the integration points with weights ω_j in the domain and $\omega^\Gamma{}_j$ on the element boundary. While Eq. (10) is a mathematical identify for any sufficiently smooth function, Eq. (11) does not in general hold. To maintain this identity, the shape function derivatives at the integration points are modified by solving a linear programming problem based on the L_2 minimization of the difference of the shape function derivatives and their original values with Eq. (11) as a constraint. Typical corrections are on the order of a few percent. These corrections are spatially local and do not require a global equation solve. Also, since a total Lagrangian formulation is used, the shape function derivatives are only corrected once, at the start of the analysis. Figure 4 shows the effect of this correction on the accuracy and convergence rate for a standard beam-bending verification problem [36] using a rectangular domain with an aspect ratio of 4.0 and a truncated regular hexagonal mesh (see Figure 5a). Without the correction, the L_2 convergence rate in the displacement field is only 1.26. With the correction, the convergence rate is 1.86 which is close to the theoretical value of 2.0 for low order isoparametric elements.

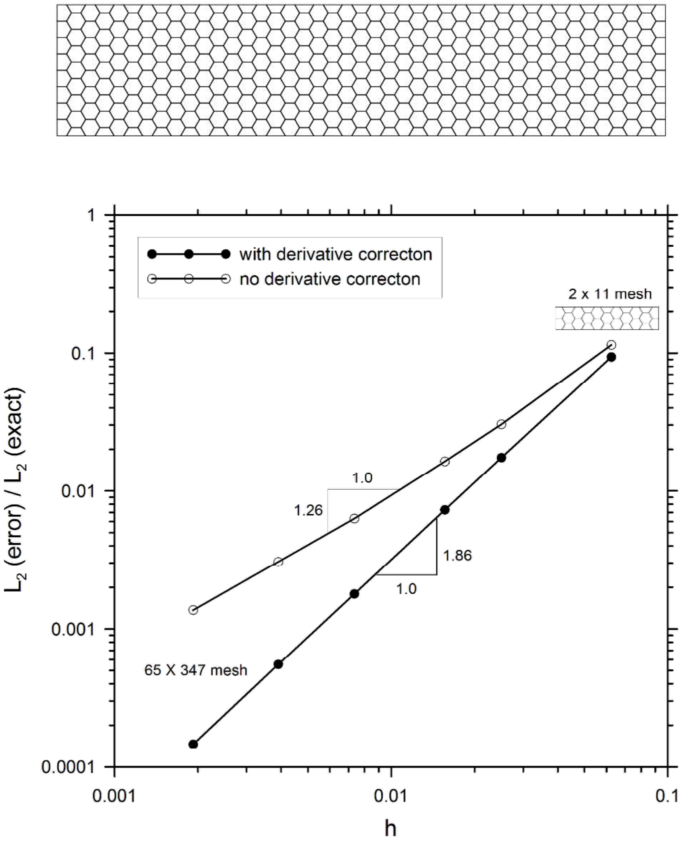

Figure 4. Effect of integration consistency on the L_2 norm of the displacement error for the beam-bending verification problem using a truncated regular hexagonal mesh shown above.

Even though there is no mapping to a parent element in the above element formulation, it is still expected that the robustness of these elements in large deformation analyses will be optimized when interior angles are maximized. For the beam-bending verification problem, there is only a slight sensitivity in the solution behavior to the shape of the elements. Figure 5b shows the L2 convergence rate in the displacement field for two random perturbations of the regular hexagonal mesh as shown in Figure 5a. To handle incompressibility, a standard mean dilation formulation is used [31,36]. Figure 6 shows the effect of Poisson's ratio on the accuracy and convergence rate of the beam-bending verification problem. The mean dilation formulation obviates any locking behavior.

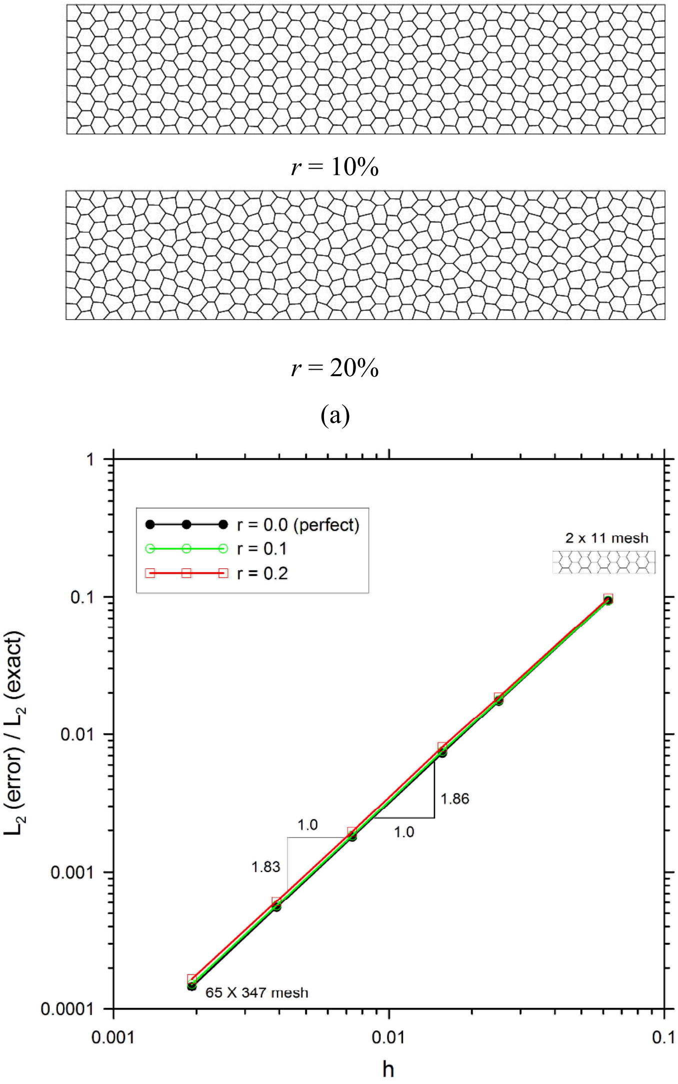

(a)

(b)

Figure 5. (a) Random perturbations in the regular hexagonal mesh in the range of r = 10% and 20% of the cell size, (b) Sensitivity of the L_2 norm of the displacement error for the beam-bending verification problem (plane stress).

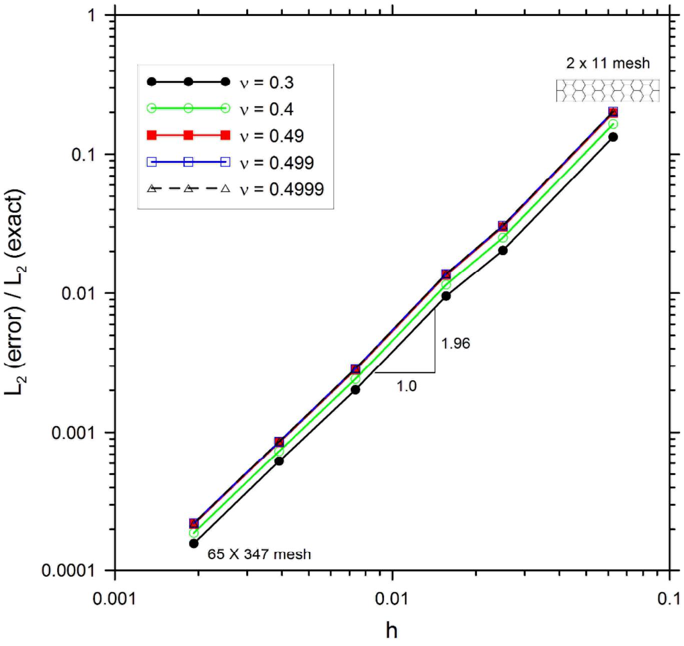

Figure 6. Effect of Poisson's ratio on the L_2 norm of the displacement error of the beam-bending verification problem (plane strain) using a mean dilation formulation with a distorted hexagonal mesh (*r* = 20%).

In the results presented so far, each element has been integrated by first triangulating the polygon by connecting each vertex and the centroid assuming that each polygon is star shaped. Standard Gauss integration is then used for each sub-triangle. The effect of number of integration points on the accuracy and convergence rate of the beam-bending verification problem (plane stress) is shown in Figure 7. The use of a minimum number of integration points (while avoiding zero-energy modes) results in increased accuracy for the plane stress case. The plane strain case exhibited an opposite effect. The subject of integration on three-dimensional polyhedral domains has been studied by Rashid [31].

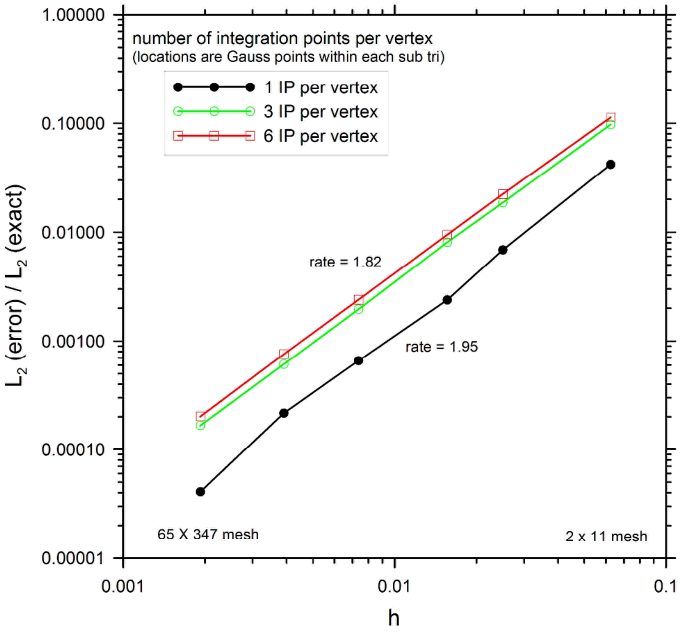

Figure 7. Effect of number of element integration points on the L_2 norm of the displacement error of the beam-bending verification problem (plane stress) with a distorted hexagonal mesh (*r* = 20%).

An explicit dynamics central difference time integration scheme [34] is used to integrate the semi-discrete equations resulting from Eq. (9). The special mass lumping procedure of Hinton [37] is used as it always produces positive lumped masses. This mass lumping procedure is recommended by Hughes for non-standard element formulations [36].

2.3 Dynamic Mesh Connectivity

Since the generation of one or more new fracture surfaces (faces in 3D, edges in 2d) can occur every time step, an efficient algorithm and data structure is needed to update the mesh connectivity as these surfaces materialize. The possible algorithms may be partitioned into two paradigms: (1) top-down modification and (2) bottom-up modification. A top-down algorithm attempts to locally modify the mesh connectivity while minimizing the overall change to the underlying data structure (see, for example, [11]). Alternatively, a bottom-up algorithm assumes that there are a large number of necessary connectivity changes per time step. The initial connectivity is completely discarded and recreated using the new fracture state. Top-down modifying algorithms are very efficient when there are a small percentage of connectivity updates but their implementation is somewhat involved. Herein, for the simulation of pervasive failure, a bottom-up modification algorithm is used. The algorithm may be described as follows. Initially, all elements are taken to be disconnected. Let the ordered pair (*a*, *i*) represent the *i*th node of the *a*th element. An equivalence relation is defined on the set of element nodes such that (*a*, *i*) and (*b*, *j*) are related if they are directly connected across an intact face (3D) or edge (2D). This equivalence relation can then be used to partition the set of element nodes into equivalence classes [38] by looping over all edges. The equivalence classes are then mapped to existing node definitions. New nodes are created as needed. This methodology has proven to be simple and robust. The generation of the element node partition structure requires only a single pass through all edge pairs (face pairs in 3D). For each edge pair, only ordinary binary lookups are required in the data structure. Thus, the overall complexity of this method is $N\log N$, where N is the number of edge pairs.

2.4 Material Failure Mechanics

For simulating pervasive failure, two methods for regularizing the governing equations and providing for a finite energy dissipation during material softening are of particular interest: (1) the dynamic insertion of cohesive tractions at the *inception* of material softening (defined by a limit or failure surface) [11-16], (2) the use of integral-form nonlocal material models [24-27,40,44] with the insertion of new crack surfaces only upon the *completion* of material softening and thus final localization of damage. The use of a nonlocal model is preferred for reasons described in reference [40]. However, its use in dynamic problems is an area of active research. In this research as a first step, the dynamic insertion of cohesive tractions is used. The dynamic insertion of cohesive tractions requires (1) a failure criterion or limit surface to indicate incipient failure and localization, (2) a traction separation law that is a function of Mode I, II, and III separation. In order to detect if the failure criterion has been obtained at the interelement faces, field quantities carried at the element integration points such as stress or internal-state variables, must be interpolated from attached elements. Once the limit state is reached at an interelement face, the connectivity of the finite-element mesh is updated as described in Section 2.3, and the cohesive traction relation is invoked. The normal tractions are taken to be zero under over-closure. The contact algorithm is used to prevent interelement penetration.

2.5 Contact Formulation

By its nature, pervasive failure involves a large amount of self-contact between crack faces. It is thus essential to have a robust contact algorithm. To avoid any constraints on surface topology that is typical of master/slave contact algorithms, a simple penalty approach is adopted. Each polyhedral element on the surface is treated independently and checked for mutual penetration as in the discrete element method [41]. Let C represent the set of elements on the instantaneous domain boundary. At the start of the simulation C is initialized with all elements on the boundary of the reference domain. As the simulation progresses and new crack surfaces nucleate, previously interior elements that are now on the boundary are added to C. Thus, the size or cardinality of C is monotonically increasing during the simulation. In the contact search phase, the elements in C are spatially sorted onto an overlayed rectangular grid based upon minimal bounding boxes. All element pairs that are 'close' are then checked for mutual penetration. If penetration is detected, a penalty force based on both the penetrating velocity and penetration is applied following Heinstein [42]. The velocity based penalty parameter was chosen to obtain 'plastic' impact conditions. The displacement based penalty parameter was chosen to be as small as possible yet still prevent gross penetration under quiescent conditions, recognizing the fact that the critical time step can be adversely affected by too large a value.

The use of spatial sorting is very efficient. Since there are no comparisons required between elements, the sorting process is order N complexity where N is the number of elements in the contact set C. If the cell size of the overlay grid is taken to be the characteristic element size, each grid cell is guaranteed to have only a few elements in each cell due to the interpenetration constraint. If the cell overlay grid is implemented as a binary tree, the overall complexity of the contact procedure is of order $N\log N$.

3 EXAMPLE

To demonstrate the proposed computational methodology for simulating pervasive failure, a 2D explicit dynamics serial code was written using the C++ programming language. The object-oriented functionality available in C++ facilitated the implementation of the computational methodology. In particular, the C++ STL library, providing the `set`, `vector`, `list`, and `map` data structures, was especially useful [39]. Implementation of the proposed computational methodology in a parallel application seems challenging due to extensive updates necessary in the mesh connectivity. It is envisioned that the research project 'phdMesh' (parallel, heterogeneous, and dynamic unstructured meshes) [43] will provide a convenient platform for developing a 3D parallel implementation.

For a simple example consider a low-strength concrete column (0.3 m by 1.83 m) impacting a rigid plane at a striking velocity of 7.6 m/s and 45° angle as shown in Figure 8. The column is idealized as a two-dimensional plane strain structure composed of an elastic material with a Mohr-Coulomb failure surface and a tensile cutoff σ_o as shown in Figure 9. The Mohr-Coulomb surface is given by

$$\left|\tau\right| = c - \mu\sigma \tag{12}$$

where τ is the limiting shear stress on a plane, σ is the normal stress on the same plane, c is the cohesion, and μ is the coefficient of internal friction. For this example, $c = \sigma_o = 3.7$ MPa and $\mu = 0.75$. For the cohesive material behavior, the bilinear model and parameters presented in reference [22] for mortar is used with an overall strain energy release rate of 57 J/m^2. The damage law is taken to be linear. Only a Mode I behavior is considered.

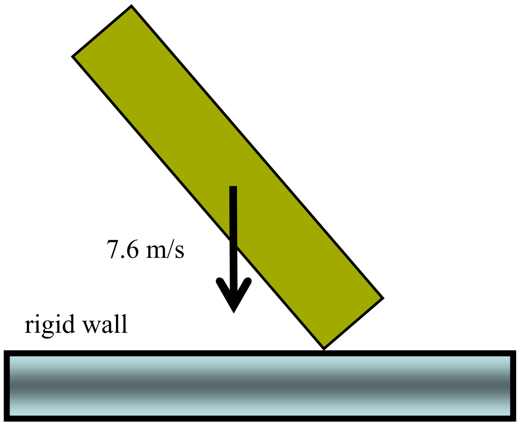

Figure 8. A rectangular column striking a rigid wall at a 45 degree angle.

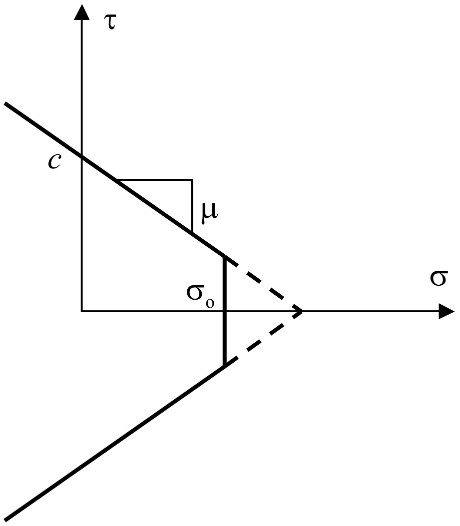

Figure 9. Mohr-Coulomb failure surface in shear (τ) normal-stress (σ) space, with cohesion *c*, tensile cutoff σ_o, and internal friction μ.

The *i*th realization of a randomly seeded Voronoi tessellation with a characteristic cell size *h* will be denoted R_i^h. Multiple realizations are shown in Figure 10a, 10b, and 10c for characteristic cell sizes 2.0 (5 cm), 1.0, and 0.5, respectively. Figure 11 shows the fracture surface for the $R_1^{0.5}$ mesh. Only fracture surfaces whose cohesive traction behavior has fully softened are shown. There is extensive fragmentation at the impact corner. Note the bending induced fracture at the midsection involving crack coalescence and branching. Figure 12 shows all fracture surfaces including those whose cohesive tractions are still active. The edge color represents the maximum achieved crack mouth opening displacement. The corresponding results for the $R_1^{0.25}$ mesh are shown in Figures 13 and 14, respectively. Note that the crack patterns are qualitatively similar but distinctly different.

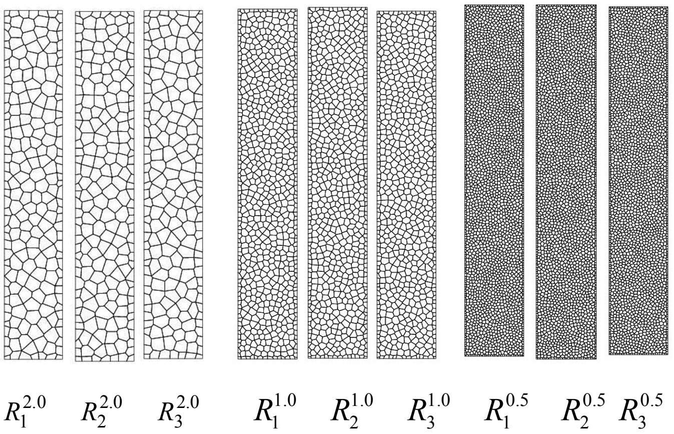

(a) $h = 2.0$ b) $h = 1.0$ (c) $h = 0.5$

Figure 10. Voronoi mesh realizations for three different characteristic cell sizes, h = 2.0, h = 1.0, and h = 0.5. Three realizations, R_1, R_2, and R_3 are shown for each characteristic cell size.

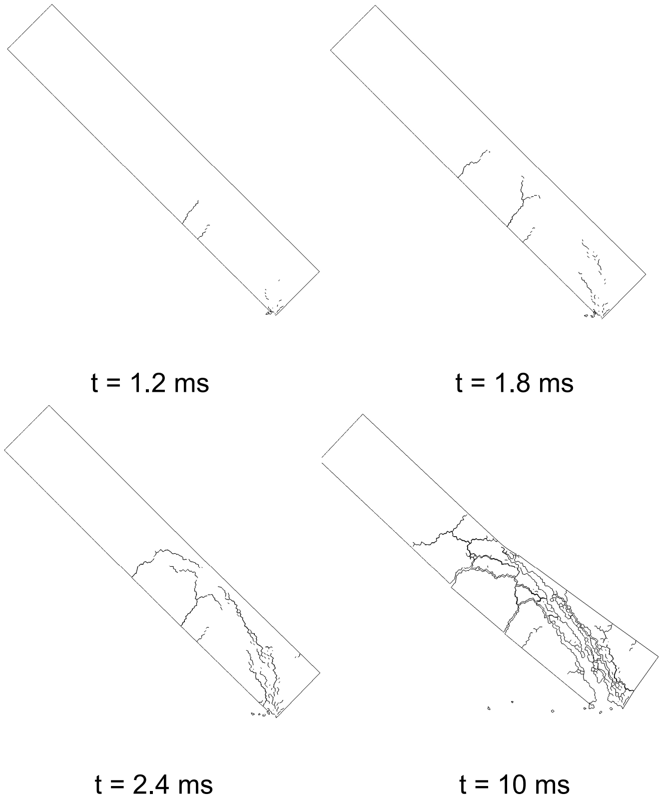

Figure 11. Deformed state of the concrete column at a number of instances in time using the $R_1^{0.5}$ mesh. Only the crack boundaries that have fully softened (no cohesive tractions) are shown.

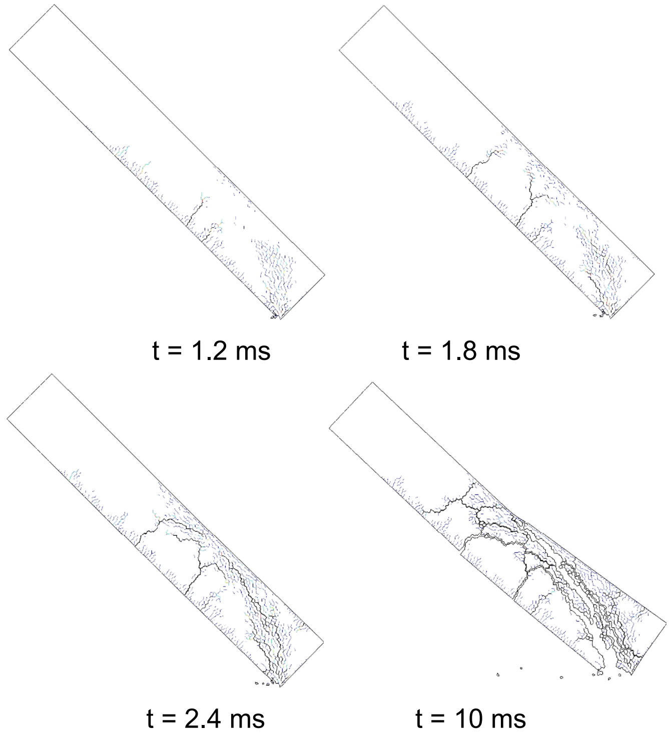

t = 1.2 ms t = 1.8 ms

t = 2.4 ms t = 10 ms

Figure 12. Deformed state of the concrete column at a number instances in time using the $R_1^{0.5}$ mesh. All new crack surfaces are shown. The crack surfaces that have cohesive tractions active are colored according to the amount of crack-mouth opening displacement (red = 25 μm).

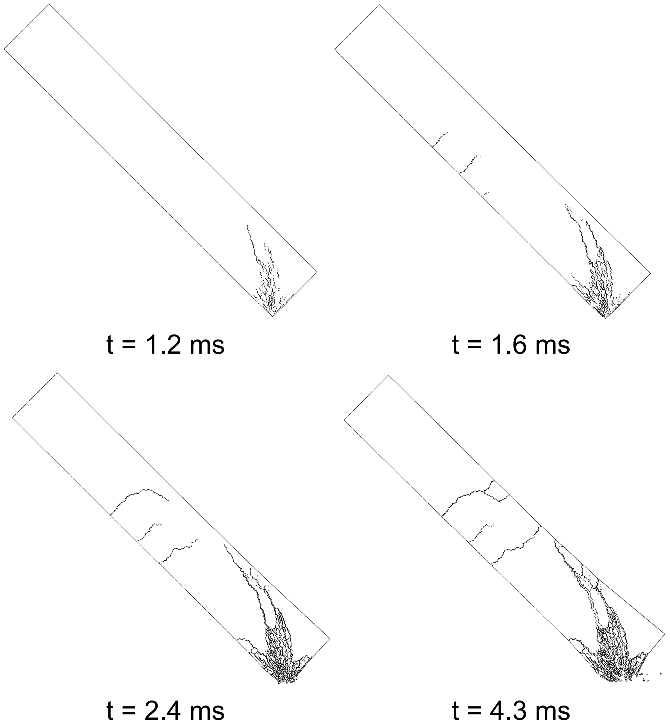

t = 1.2 ms t = 1.6 ms

t = 2.4 ms t = 4.3 ms

Figure 13. Deformed state of the concrete column at a number of instances in time using the $R_1^{0.25}$ mesh. Only the crack boundaries that have fully softened (no cohesive tractions) are shown.

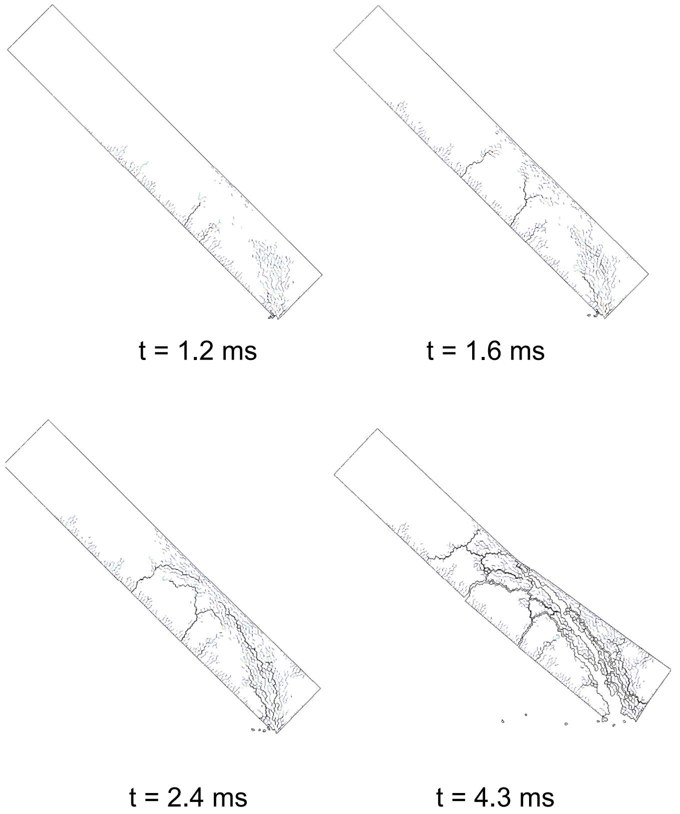

t = 1.2 ms t = 1.6 ms

t = 2.4 ms t = 4.3 ms

Figure 14. Deformed state of the concrete column at a number instances in time using the $R_1^{0.25}$ mesh. All new crack surfaces are shown. The crack surfaces that have cohesive tractions active are colored according to the amount of crack-mouth opening displacement (red = 25 μm).

The maximum principal stress field at a simulation time of 50 ms is shown in Figure 15 for the $R_1^{2.0}$, $R_2^{2.0}$, and $R_3^{2.0}$ meshes. The crack patterns are qualitatively similar but distinctly different. The corresponding results for the $R_1^{1.0}$, $R_2^{1.0}$, and $R_3^{1.0}$ meshes are shown in Figure 16. The corresponding results for the $R_1^{0.5}$, $R_2^{0.5}$, and $R_3^{0.5}$ meshes are shown in Figure 17. Finally, the corresponding results for the $R_1^{0.25}$, $R_2^{0.25}$, and $R_3^{0.25}$ meshes are shown in Figure 18. Note that at all refinement levels, the fracture patterns are qualitatively similar, but distinctly different. Since the material properties are completely homogeneous, this difference in crack patterns represents a type of mesh dependence, albeit unbiased. In a sense, the random Voronoi edge orientations provide an implicit variation in the underlying fracture properties of the material.

For this class of problems, in which a multitude of bifurcations exist in the physical response, a weaker notion of convergence is more appropriate. It is proposed that engineering 'quantities of interest' should be described in terms of distributions, commonly referred to as 'weak convergence' or 'convergence in variation' in the statistical community [45]. Possible engineering quantities of interest include the extent and nature of cracking, fragment-size distributions, and post-failure structural response. The cumulative distribution of fragment size at the simulation time of 300 ms is shown in Figure 19 for twelve mesh realizations $R_i^{0.5}$, $i \in \{1,2,3,\ldots,12\}$. Note that each distribution is distinctly different. Again, since the material properties are completely homogeneous, the difference in fragment distributions represents a type of mesh dependence, albeit unbiased. The corresponding results for the $R_i^{0.25}$ mesh family are shown in Figure 20. While twelve realizations is a small sample size for what is expected to be a complex statistical distribution for fragment size, it is clear that the distribution of cumulative distributions has not 'converged'.

The *maximum* fragment size for each mesh realization at a simulation time of 300 ms is shown in Figure 21. Results are given for the mesh resolutions $R_i^{2.0}$, $R_i^{1.0}$, $R_i^{0.5}$, and $R_i^{0.25}$. Convergence of this engineering quantity-of-interest is again not apparent. Clearly, more research remains, and the challenge of defining what is meant by 'convergence' for problems exhibiting a multitude of bifurcations is apparent.

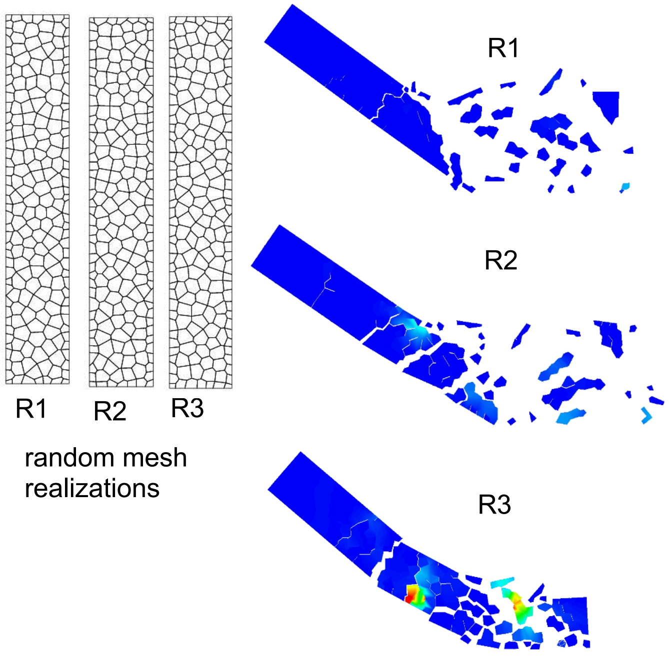

Figure 15. Maximum principal stress field at a simulation time of 50 ms for the $R_1^{2.0}$, $R_2^{2.0}$, and $R_3^{2.0}$ mesh realizations.

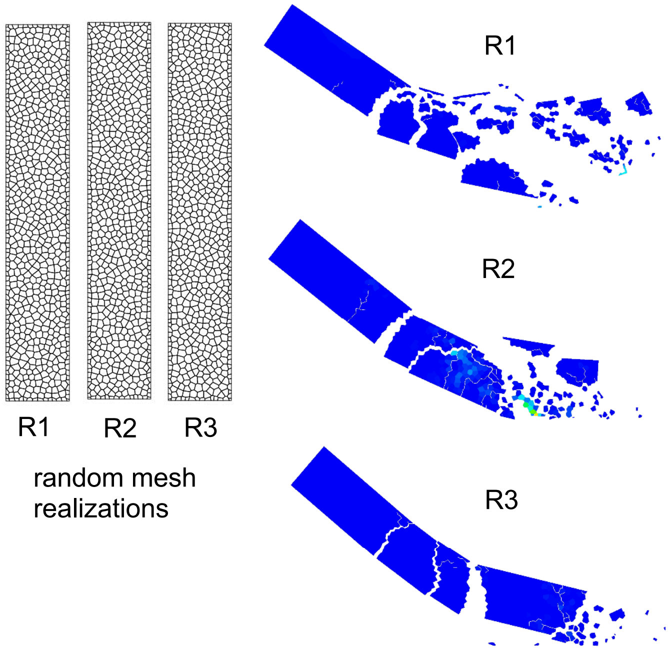

Figure 16. Maximum principal stress field at a simulation time of 50 ms for the $R_1^{1.0}$, $R_2^{1.0}$, and $R_3^{1.0}$ mesh realizations.

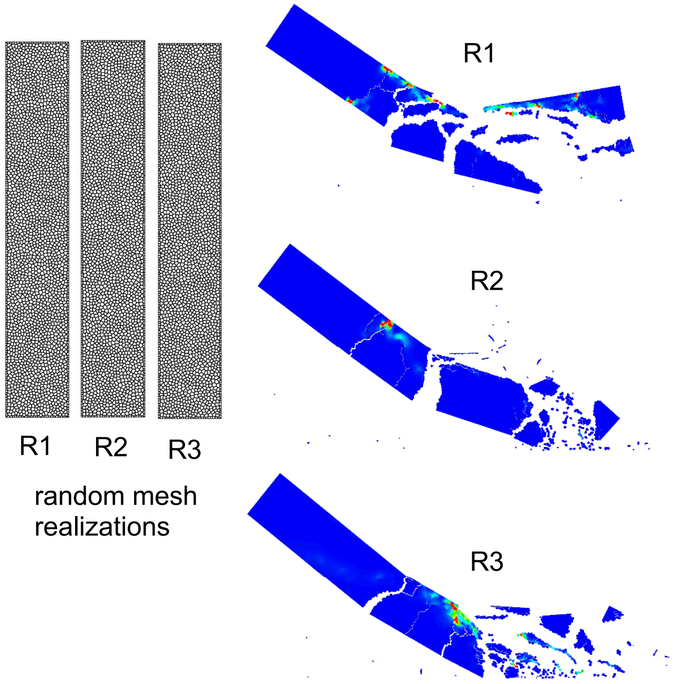

Figure 17. Maximum principal stress field at a simulation time of 50 ms for the $R_1^{0.5}$, $R_2^{0.5}$, and $R_3^{0.5}$ mesh realizations.

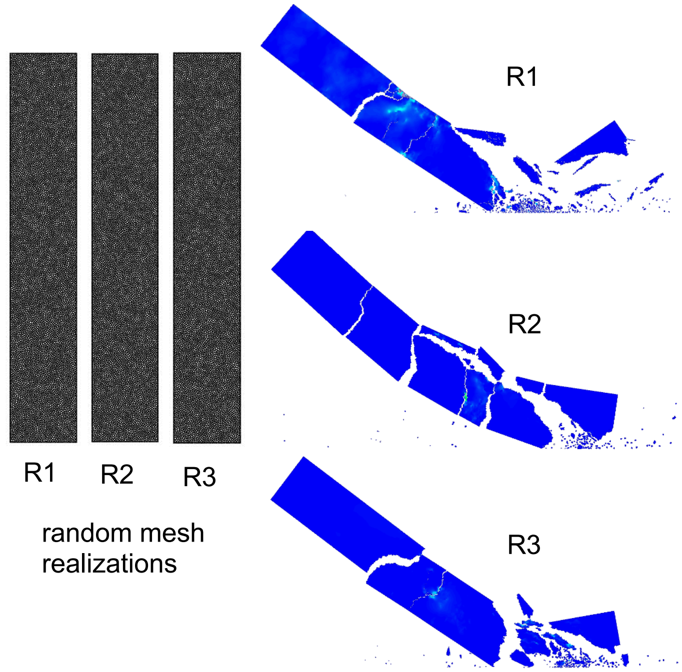

Figure 18. Maximum principal stress field at a simulation time of 50 ms for the $R_1^{0.25}$, $R_2^{0.25}$, and $R_3^{0.25}$ mesh realizations.

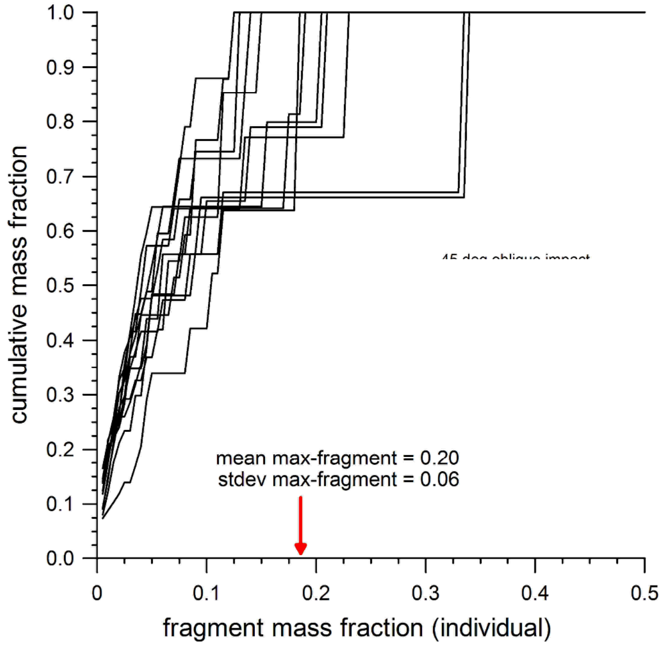

Figure 19. Cumulative distribution of the fragment mass-fraction at a simulation time of 300 ms for the $R_i^{0.5}$, $i \in \{1,2,3,\ldots,12\}$ mesh family. The mean of the maximum-fragment mass-fraction is denoted by the arrow. The standard deviation of the maximum fragment mass-fraction is given as well.

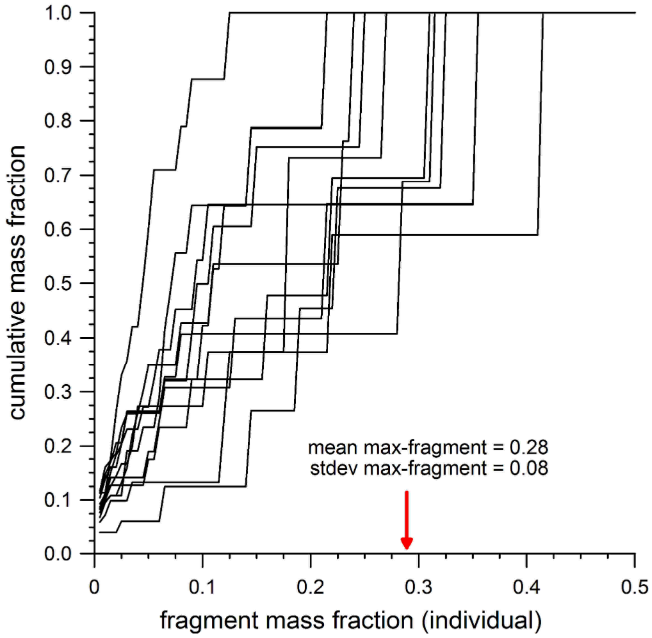

Figure 20. Cumulative distribution of the fragment mass-fraction at a simulation time of 300 ms for the $R_i^{0.25}$, $i \in \{1,2,3,\ldots,12\}$ mesh family. The mean of the maximum-fragment mass-fraction is denoted by the arrow. The standard deviation of the maximum fragment mass-fraction is given as well.

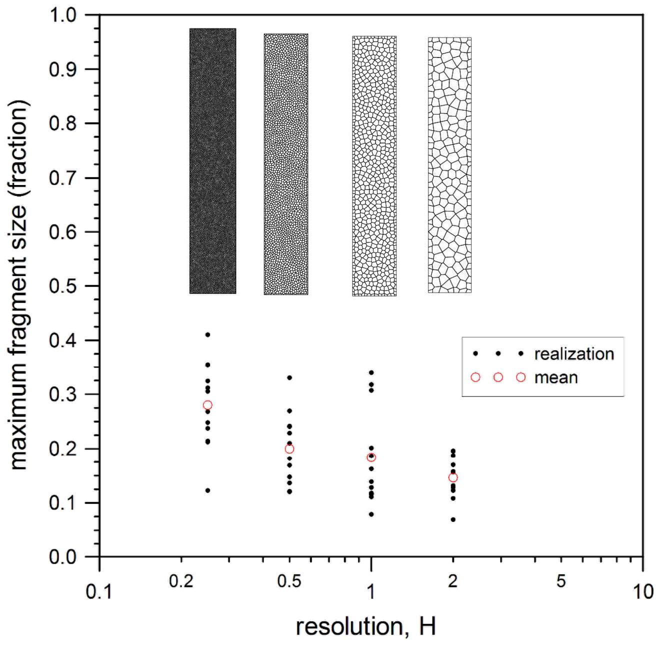

Figure 21. The maximum fragment size for twelve mesh realizations at four characteristic mesh sizes $R_i^{2.0}$, $R_i^{1.0}$, $R_i^{0.5}$, and $R_i^{0.25}$. The mean of the maximum fragment mass-fraction is given as well.

To highlight the effect of explicit material property variation on the fracture process, the simulations for the $R_1^{0.5}$ mesh where performed with a 5% uniform variation in elastic modulus and the internal friction μ. Twelve realizations of material properties were produced. The resulting cumulative fragment distributions are shown in Figure 22. The result for the nominal material properties (homogenous case) is also given. Note that the variability in the fragment distributions is similar to that for the multiple mesh realizations but with homogenous material properties, as hypothesized earlier. Future work will focus on including *spatially correlated* variations in the element edge fracture properties directly into the simulation as a possible approach for removing the observed mesh dependence.

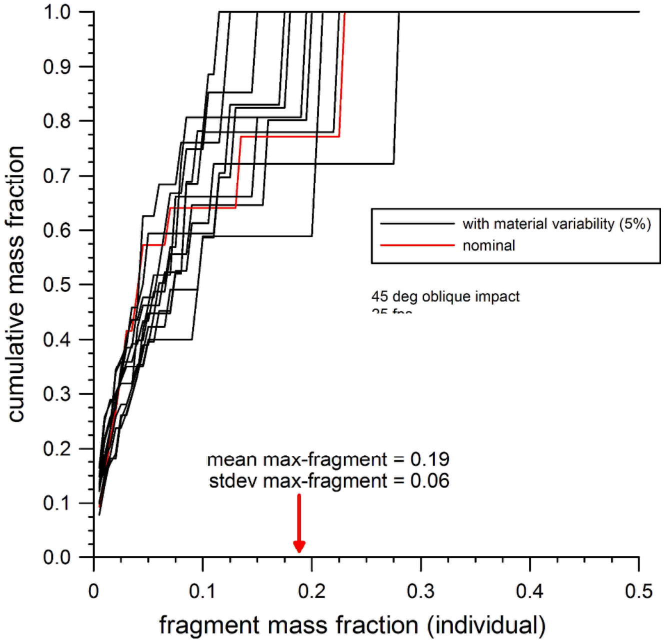

Figure 22. Cumulative distribution of the fragment mass-fraction at a simulation time of 300 ms for the $R_1^{0.5}$ mesh using a 5% element variation on elastic modulus and Mohr-Coulomb failure surface. The homogenous (nominal) case is given for comparison.

4 CHALLENGES AND NEXT STEPS

The proposed computational methodology for simulating the pervasive failure of structures is promising. However, much work remains in demonstrating convergence and ultimately that the methodology is objective with respect to mesh refinement. Due to the physical nature of the class of problems, with a multitude of bifurcations, it is unclear how to even define convergence, which is necessary condition for objectivity. The statistical concept of 'weak convergence' was proposed. The use of a non-local model (integral form) instead of the dynamic insertion of cohesive tractions is probably more appropriate for this class of problems (as opposed to single crack propagation). However, their application to dynamic problems is in the preliminary stages of research. There are a number of validation problems that are currently being analyzed with this methodology including cylindrical and prismatic Brazilian experiments, and three and four point bend experiments.

REFERENCES

[1] Strouboulis, T., Copps, K., and Babuska, I. (2000) 'The Generalized Finite Element Method: An Example of its Implementation and Illustration of its Performance,' *International Journal for Numerical Methods in Engineering*, 47, 1401-1417.

[2] Belytschko, T. and Black, T. (1999) 'Elastic Crack Growth in Finite Elements with Minimal Remeshing,' *International Journal for Numerical Methods in Engineering*, 45, 601-620.

[3] Belytschko, T., Krongauz, Y., Organ, D., Flemin, M., and Krysl, P. (1996) 'Meshless Melthods: An Overview and Recent Developments,' *Computer Methods in Applied Mechanics and Engineering*, 139, 3-47.

[4] Attaway, S., Heistein, M., and Swegle, J. (1994) 'Coupling of Smooth Particle Hydrodynamics with the Finite Element Method,' *Nuclear Engineering and Design*, 150, 199-205.

[5] Belytschko, T., Krysl, P., and Krongauz, Y. (1997) 'A Three-Dimensional Explicit Element-Free Galerkin Method,' *International Journal for Numerical Methods in Fluids*, 24, 1253-1270.

[6] Liu, W.K., Jun, S., and Zhang, Y.F. (1995) 'Reproducing Kernel Particle Methods,' *International Journal for Numerical Methods in Engineering*, 20, 1081-1106.

[7] Rabczuk, T. and Belytschko, T. (2004) 'Cracking Particles: A Simplified Meshfree Method for Arbitrary Evolving Cracks,' *International Journal for Numerical Methods in Engineering*, 61, 2316-2343.

[8] Silling, S. and Askari, E. (2005) 'A Meshfree Method Based on the Peridynamic Model of Solid Mechanics,' *Computers and Structures*, 83, 1526-1535

[9] Park, Y.K. and Fahrenthold, E. (2005) 'A Kernel Free Particle-Finite Element Method for Hypervelocity Impact Simulation,' *International Journal for Numerical Methods in Engineering*, 63, 737-759.

[10] Johnson, G., Beissel, S. and Stryk, R. (2002) 'An Improved Generalized Particle Algorithm that Includes Boundaries and Interfaces,' *International Journal for Numerical Methods in Engineering*, 53, 875-904.

[11] Pandolfi, A. and Ortiz, M. (2002) 'An Efficient Adaptive Procedure for Three-Dimensional Fragmentation Simulations,' *Engineering with Computers*, 18, 148-159.

[12] Pandolfi, A., Krysl, P., and Ortiz, M. (1999) 'Finite Element Simulation of Ring Expansion and Fragmentation: the Capturing of Length and Time Scales through Cohesive Models of Fracture,' *International Journal of Fracture*, 95, 279-297.

[13] Ruiz, G., Ortiz, M., and Pandolfi, A. (2000) 'Three-Dimensional Finite-Element Simulation of the Dynamic Brazilian Test on Concrete Cylinders,' *International Journal for Numerical Methods in Engineering*, 48, 963-994.

[14] Camacho, G. and Ortiz, M. (1996) 'Computational Modeling of Impact Damage in Brittle Materials,' *International Journal of Solids and Structures*, 33, 2899-2938.

[15] Ruiz, G., Pandolfi, A., and Ortiz, M. (2001) 'Three-Dimensional Cohesive Modeling of Dynamic Mixed-Mode Fracture,' *International Journal for Numerical Methods in Engineering*, 52, 97-120

[16] Ortiz, M. and Pandolfi, A. (1999) 'Finite-Deformation Irreversible Cohesive Elements for Three-Dimensional Crack-Propagation Analysis,' *International Journal for Numerical Methods in Engineering*, 44, 1267-1282.

[17] Bolander, J.E., Saito, S. (1998) 'Fracture Analyses using Spring Networks with Random Geometry,' *Engineering Fracture Mechanics*, 61, 569-591

[18] Bolander, J.E. and Sukumar, N. (2005) 'Irregular Lattice Model for Quasistatic Crack Propagation,' *Physical Review B*, 71, 094106-1:12.

[19] Yip, M., Mohle, J, and Bolander, J.E. (2005) 'Automated Modeling of Three-Dimensional Structural Components Using Irregular Lattices,' *Computer-Aided Civil and Infrastructure Engineering*, 20, 393-407.

[20] Yip, M., Li, Z., Liao, B.S., and Bolander, J.E., (2006) 'Irregular Lattice Models of Fracture of Multiphase Particulate Materials,' *International Journal of Fracture*, 140, 113-124.

[21] Bazant, Z.P. and Planas, J. (1997) 'Fracture and Size Effect in Concrete and other Quasibrittle Materials,' CRC Press.

[22] Planas, J., Elices, M., Guinea, G., Gomez, F., Cendon, D. and Arbilla, I. (2003) 'Generalizations and Specializations of Cohesive Crack Models,' *Engineering Fracture Mechanics*, 70, 1759-1776

[23] Jirasek, M. (1998) 'Nonlocal Models for Damage and Fracture: Comparison of Approaches,' International Journal of Solids and Structures, 35, 4133-4145.

[24] Planas, J., Elices, M., and Guinea, G. (1993) 'Cohesive Cracks Versus Nonlocal Models: Closing the Gap,' *International Journal of Fracture*, 63, 173-187.

[25] Jirasek, M. and Rolshoven, S. (2003) 'Comparison of Integral-Type Nonlocal Plasticity Models for Strain-Softening Materials,' *International Journal of Engineering Science*, 41, 1553-1602.

[26] Grassl, P. and Jirasek, M. (2006) 'Damage-Plastic Model for Concrete Failure,' *International Journal of Solids and Structures*, 43, 7166-7196.

[27] Grassl, P. and Jirasek, M. (2006) 'Plastic Model with Non-Local Damage Applied to Concrete,' *International Journal of Numerical and Analytical Methods in Geomechanics*, 30, 71-90.

[28] Okabe, A., Boots, B., Sugihara, K., and Chiu, S.N. (2000) *Spatial Tessellations: Concepts and Applications of Voronoi Diagrams*, John Wiley & Sons.

[29] Bowyer, A. (1981) 'Computing Dirichlet Tessellations,' *The Computer Journal*, 2, 162-166.

[30] Watson, D. (1981) 'Computing the n-Dimensional Tessellation with Application to Voronoi Polytopes,' *The Computer Journal*, 2, 167-172.

[31] Rashid, M. and Selimotic, M. (2006) 'A Three-Dimensional Finite Element Method with Arbitrary Polyhedral Elements,' *International Journal for Numerical Methods in Engineering*, 67, 226-252.

[32] Idelsohn, S., Onate, E., Calvo, N., and Pin, F. (2003) 'The Meshless Finite Element Method,' *International Journal for Numerical Methods in Engineering*, 58, 893-912.

[33] Wachspress, E. (1975) *A Rational Finite Element Basis*, Academic Press.

[34] Belytschko, T., Liu, W.K., and Moran, B. (2000) *Nonlinear Finite Elements for Continua and Structures*, John Wiley and Sons.

[35] Chen, J.S., Wu, C.T., Yoon, S., and You, Y. (2001) 'A Stabalized Conforming Nodal Integration for Galerkin Mesh-Free Methods,' *International Journal for Numerical Methods in Engineering,* 50, 435-466.

[36] Hughes, T.J.R. (1987) *The Finite Element Method: Linear Static and Dynamic Finite Element Analysis*, Prentice-Hall.

[37] Hinton, E., Rock, T., and Zienkiewicz, O.C. (1976) 'A Note on Mass Lumping and Related Processes in the Finite Element Method,' *Earthquake Engineering and Structural Dynamics*, 4, 245-249.

[38] Gallian, J. (1994) *Contemporary Abstract Algebra 3rd edition*, D.C Heath and Company.

[39] Josuttis, N. (1999) *The C++ Standard Library: A Tutorial and Reference*, Addison-Wesley.

[40] Bazant, Z.P. and Jirasek, M. (2002) 'Nonlocal Integral Formulations of Plasticity and Damage: Survey of Progress,' *Journal of Engineering Mechanics*, 128, 1119-1149.

[41] Mohammadi, S. (2003) *Discontinuum Mechanics: Using Discrete and Finite Elements*, WIT Press.

[42] Heinstein, M., Mello, F., Attaway, S., and Laurson, T. (2000) 'Contact-Impact Modeling in Explicit Transient Dynamics,' *Computer Methods in Applied Mechanics and Engineering,* 187, 621-640.

[43] Edwards, H. (2007) 'An HPC Component for Parallel, Heterogeneous, and Dynamic Unstructures Meshes,' *HPC-GECO/CompFrame 2007*, Montreal, Canada.

[44] Chen, E.P. (1999) 'Non-Local Effects on Dynamic Damage Accumulation in Brittle Solids,' *International Journal of Numerical and Analytical Methods in Geomechanics*, 23, 1-21.

[45] Bremaud, P. (1999) *Markov Chains, Gibbs Fields, Monte Carlo Simulation, and Queues*, Springer.

[46] Ghosh, S. and Mallett, R. (1994) 'Voronoi Cell Finite Elements,' *Computers and Structures*, 50, 33-46.

[47] Moorthy, S. and Ghosh, S. (1996) 'A Model for Analysis of Arbitrary Composite and Porous Microstructures with Voronoi Cell Finite Elements,' *International Journal for Numerical Methods in Engineering*, 39, 2363-2398.

[48] Hu, C., Bai, J., and Ghosh, S. (2007) 'Micromechanical and Macroscopic Models of Ductile Fracture in Particle Reinforced Metallic Structures,' *Modelling and Simulation in Materials Science and Engineering*, 15, 1-16.